Journal of Materials Chemistry A

Electro-Chemo-Mechanical Evolution of Sulfide Solid Electrolyte/Li Metal Interfaces: Operando analysis and ALD Interlayer Effects

Journal:	*Journal of Materials Chemistry A*
Manuscript ID	TA-ART-10-2019-011508.R2
Article Type:	Paper
Date Submitted by the Author:	26-Feb-2020
Complete List of Authors:	Davis, Andrew; University of Michigan, Mechanical Engineering Garcia-Mendez, Regina; University of Michigan, Department of Materials Science & Engineering Wood, Kevin; San Diego State University, Mechanical Engineering Kazyak, Eric; University of Michigan, Mechanical Engineering Chen, Kuan-Hung; University of Michigan, Materials Science and Engineering Teeter, Glenn; National Renewable Energy Laboratory, Sakamoto, Jeffrey ; University of Michigan, Mechanical Engineering Dasgupta, Neil; University of Michigan, Mechanical Engineering

SCHOLARONE™
Manuscripts

ARTICLE

Electro-Chemo-Mechanical Evolution of Sulfide Solid Electrolyte/ Li Metal Interfaces: *Operando* analysis and ALD Interlayer Effects

Received 00th January 20xx,
Accepted 00th January 20xx

DOI: 10.1039/x0xx00000x

Andrew L. Davis[a], Regina Garcia-Mendez[b], Kevin N. Wood[c,d], Eric Kazyak[a], Kuan-Hung Chen[b], Glenn Teeter[c], Jeff Sakamoto[a,b], Neil P. Dasgupta*[a]

Sulfide solid electrolyte (SE) materials show promise for high-performance solid-state batteries because of their high ionic conductivity and ease of processing. However, sulfide electrolytes have suffered from chemical and electrochemical instability against Li metal anodes. Herein, we use a suite of *operando* microscopy and spectroscopy techniques to study the impact of artificial solid electrolyte interphases (SEI) on the electro-chemo-mechanical degradation of sulfide solid electrolytes. Al_2O_3 interlayers deposited using atomic layer deposition (ALD) are used as a model system to show that the application of artificial SEI interlayers can delay degradation at the Li/LGPS interface by modifying the solid electrolyte interphase chemistry and morphology. Optical and scanning electron microscopy are used to rationalize the electrochemical response of the system, which is attributed to a delayed onset of mechanical degradation at the interface when ALD interlayers are used. *Operando* X-ray photoelectron spectroscopy demonstrates that the dynamic evolution of SEI chemistry is impacted by the presence of the ALD interlayer. Auger electron spectroscopy and *operando* optical microscopy provide visual evidence of spatial heterogeneity of Li plating, which is attributed to the chemo-mechanical degradation of the ALD interphase. The implications of these observations provide valuable insights toward the development of robust interlayers for solid-state batteries.

Introduction

Li-ion batteries have transformed energy storage across sectors ranging from personal electronics to electric vehicles. Batteries with longer lifetimes, higher capacities, and improved safety have the potential to continue this transformation and accelerate our transition to renewable energy. Solid-state batteries are one of the most promising technologies to move beyond Li-ion because they eliminate the need for flammable liquid electrolytes and have the potential to enable next-generation chemistries such as Li-sulfur and Li-air.[1,2] Li metal anodes are a critical component for these high-energy-density systems, but extended cycling of Li metal anodes in liquid electrolytes has proven elusive. Conversely, several solid-state batteries have exhibited stable cycling of Li metal anodes up to thousands of cycles.[3,4]

Sulfide solid electrolyte (SE) materials have shown particular promise for high performance solid-state batteries because of their high ionic conductivities, which are comparable to or higher than that of liquid electrolytes.[5–8] Previous efforts have shown that sulfide SEs are compatible with room temperature processing and can enable fast charging in full cells.[9,10] Despite this promise, sulfide SEs have a narrow electrochemical stability window, which causes degradation at the Li metal/SE interface. This degradation leads to high interfacial impedance and eventual cell failure.[11–14]

The decomposition of sulfide SEs, and corresponding formation of a solid electrolyte interface (SEI) after contact with Li metal, has been characterized by various experimental and computational techniques, including x-ray photoelectron spectroscopy (XPS), Raman spectroscopy, x-ray diffraction, and density functional theory modeling.[15–18] Two distinct types of SEI chemistry have been observed.[19–21] The first is an electronically insulating SEI such as that formed at the Li/Li_2S-P_2S_5 (LPS) interface, which decomposes Li_2S and Li_3P.[15] After initial SEI formation, further transport of electrons to the SEI/SE interface is limited, leading to a kinetically stable interface. The second type of SEI chemistry is a mixed electronic/ionic conducting interface, such as that formed by $Li_{10}GeP_2S_{12}$ (LGPS), which is formed of Li_3P, Li_2S, and an electronically conducting Li–Ge alloy ($Li_{15}Ge_4$).[12,22–24] In this mixed conducting case electronic conductivity allows for electron transport to the SEI/SE interface even after initial SEI formation, leading to continued decomposition of the electrolyte.

One approach that has been proposed for stabilizing the sulfide electrolyte/Li-metal interface is the introduction of an artificial SEI by deposition of thin-film interlayers. An ideal artificial SEI layer would mirror a kinetically stable SEI, which is ionically conductive but electronically insulating.[12,25] In addition, it would exhibit a wide electrochemical window, low charge-transfer resistance at both the electrode and electrolyte

[a] Department of Mechanical Engineering, University of Michigan, Ann Arbor. E-mail: ndasgupt@umich.edu
[b] Department of Materials Science and Engineering, University of Michigan, Ann Arbor.
[c] Materials Science Center, National Renewable Energy Laboratory.
[d] Department of Mechanical Engineering, San Diego State University.
Electronic Supplementary Information (ESI) available. See DOI: 10.1039/x0xx00000x

interfaces, and it would be mechanically robust to allow volume changes upon charging/discharging to occur without degradation. Several recent studies that incorporate artificial SEI layers have observed decreases in interfacial degradation at low current densities (<1 mA/cm^2).[26–30]

One technique that has proven to be effective for the fabrication of artificial SEIs in various liquid and solid-state electrolyte systems is atomic layer deposition (ALD).[31–36] ALD is a modified chemical vapor deposition processes that conformally deposits thin (0.1-100 nm) films of a wide range of materials with atomically-precise control of thickness and composition.[37–39] This fine control of thickness and composition allows for atomically-precise control of artificial SEI interlayers.

As one of the most well-behaved, low temperature ALD processes, ALD Al_2O_3 has received particular attention as an interlayer in both liquid and solid-state battery systems. In liquid electrolyte systems, ALD Al_2O_3 has been shown to improve interface stability of both Li metal anodes and high voltage cathodes.[31,40–44] In solid state systems, ALD Al_2O_3 has also been shown to decrease improve by improving the wettability between Li metal/solid electrolyte interfaces.[36]

In the past several years, initial efforts have begun to explore ALD interlayers for stabilizing the Li-metal interface in sulfide SE systems. Two recent studies in particular have explored directly depositing ALD Al_2O_3 layers onto the surface of Li metal foils, which were subsequently brought into contact with the sulfide SE.[45,46] While improvements in interfacial stability were observed, interfacial impedance in ALD Al_2O_3 coated Li metal was reported to increase during cycling. It was proposed that mechanical degradation of the ALD Al_2O_3 layer may play a role in the eventual degradation of the interlayer during cycling.[45] This proposed mechanism is consistent with the observation that ALD Al_2O_3 coatings on Li metal can experience fracture under tensile stresses.[47] Therefore, an improved understanding of the dynamic mechanisms and the coupled electro-chemo-mechanical evolution of ALD Al_2O_3 interlayers during cycling is important to the future development of artificial SEI layers. As a well behaved ALD process which has been investigated as an artificial SEI interlayer, ALD Al_2O_3 is an ideal model system for understanding the impact and failure mechanisms of artificial SEI.

In this work, we apply a multi-modal characterization approach to understand the impact of ALD interlayers on interfacial degradation of the LGPS/Li metal interface. We demonstrate that direct deposition of Al_2O_3 interlayers onto an LGPS surface delays interfacial degradation by modifying the dynamic evolution of SEI chemistry and morphology as the electrolyte first comes into contact with Li. Electrochemical measurements of the ALD-coated samples indicate a delay in SEI growth and corresponding increase in interfacial impedance. Optical and scanning electron microscopy show that SEI formation and growth leads to mechanical degradation of the interface and confirm that ALD interlayers delay interfacial degradation. Additionally, *operando* x-ray photoelectron spectroscopy (opXPS) was used to probe differences in the chemistry of the SEI in coated and uncoated samples. Auger electron spectroscopy (AES) and *operando* optical video microscopy demonstrate the chemo-mechanical breakdown of the ALD interlayer, which leads to heterogeneous Li plating and eventual breakdown of the LGPS. These results provide insight into the mechanisms behind eventual failure of artificial SEI layers, and highlight the importance of mechanical properties in the development of future interlayers.

Results and Discussion

Li-Li Symmetric Cells

To probe the Li/LGPS interface, Li-Li symmetric cells with and without ALD coatings were assembled as shown in Figure 1a. 20 nm of Al_2O_3 was directly coated onto LGPS surfaces inside of an argon glovebox-integrated ALD system, allowing for surface modification and electrochemical testing without any air exposure. The ALD/LGPS interface was examined using cross sectional SEM and XPS depth profiling as shown in the supporting information (Figure S1, S2). Electrochemical impedance spectroscopy (EIS) and post-mortem microscopy of these cells under open circuit conditions were used to study the effects of ALD interlayers on interfacial degradation. To study the dynamic evolution of the interface under cycling, a complementary set of Li-Li symmetric cells were cycled at 0.1 mA/cm^2 and the voltage traces between the coated and uncoated samples were compared (Figure 1e).

Uncoated Li-Li Symmetric Cell. EIS analysis of uncoated samples immediately after assembly indicated LGPS conductivities of 3-4 mS/cm, which is comparable to those found in literature (Figure 1b).[5,22,26,27] A continuous increase in impedance over time at open circuit was measured by EIS (Figure 1c). The interface did not stabilize, even after several days of Li contact, after which time the impedance had increased by more than an order of magnitude. Similarly, in the uncoated cell that was cycled (Figure 1e), the voltage trace steadily increased throughout cycling (Figure 1e). The increasing impedance seen in both the cycled and un-cycled (open circuit) cells is attributed to the reduction of LGPS, which results in continual evolution of the SEI layer.

Disassembly and post-mortem optical microscopy of the open circuit cells provided evidence of LGPS reduction. Although Li metal initially adheres strongly to the LGPS surface, after 1 hr, the interface degraded to the point that the Li was easily removed from the surface, which resulted in significant visual darkening (Figure 2b). After 10 hr of Li contact, the extent of this degradation increased, resulting in a surface with a larger density of reduction products (Figure 2c). Higher magnification images show that darkening is caused by black spots uniformly scattered across the surface. SEM images of the interface (Figure 2g-h) revealed that within the black spots, the surface is pitted, leaving a highly textured and fragmented surface. Figure S5 contains optical images of the Li after removal from the LGPS and reveals that in these pitted regions of the LGPS, significant SEI debris is left attached to the Li.

The pitting and texturing of the surface is attributed to mechanical fracture of the LGPS. A recent study showed that

This journal is © The Royal Society of Chemistry 20xx

Please do not adjust margins

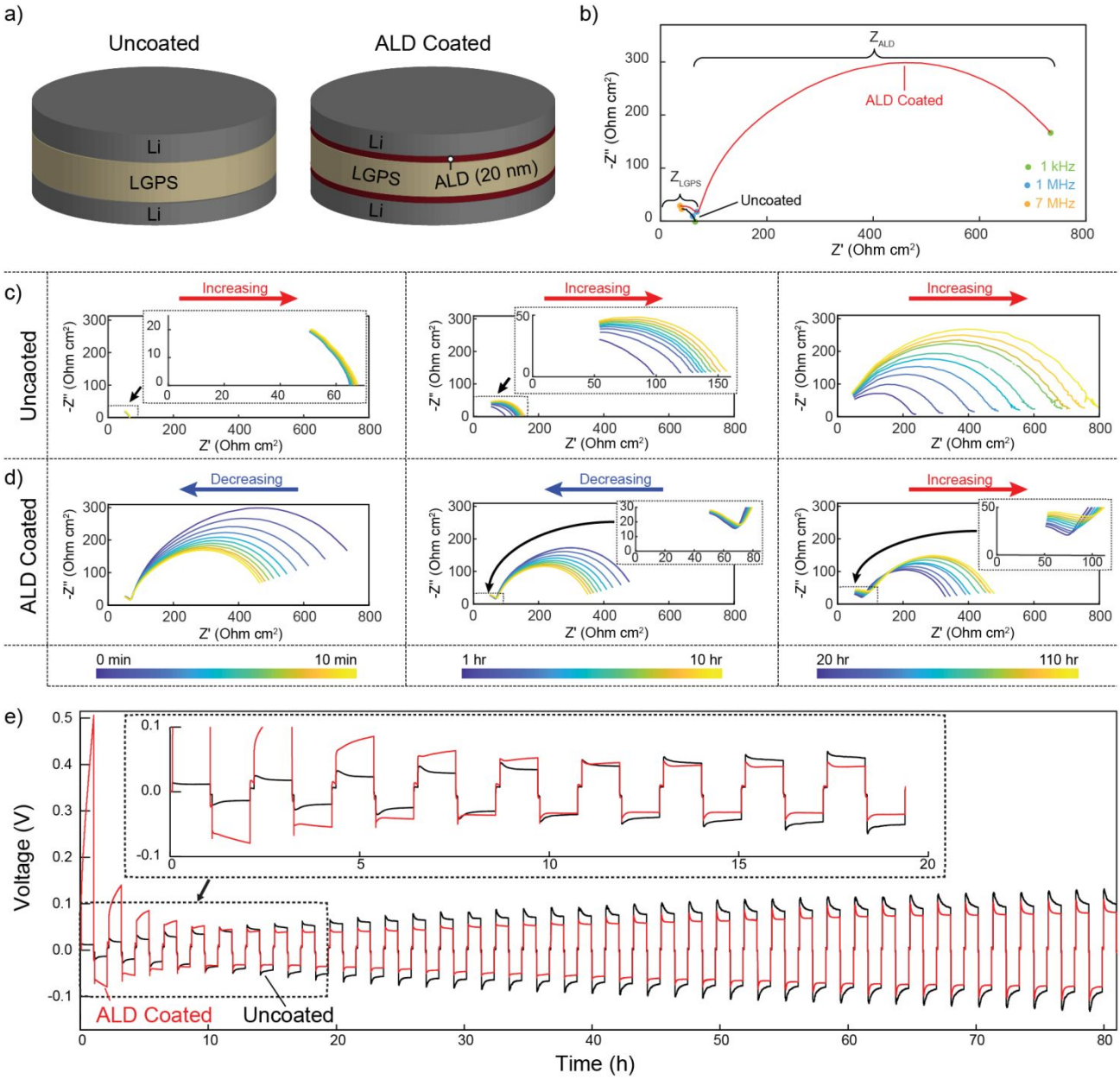

Figure 1. (a) Schematic of uncoated and ALD coated Li-Li symmetric cells. (b) Nyquist plot of the uncoated and ALD coated samples immediately after assembly. All EIS was performed at 26 °C. (c,d) EIS measurements of impedance over several time scales in both the coated and uncoated samples. Fitted impedance over time for each of the semicircles are shown in the supporting information (Figure S3). e) Voltage traces of uncoated and ALD-coated Li-Li symmetric cells during cycling. During each half cycle 0.1 mAh/cm² (~0.44 µm) of Li was plated at a constant current of 0.1 mA/cm². Comparisons between early and late cycle voltage traces are shown in the supporting information (Figure S4)

sulfide SEs can expand significantly as they are reduced (in some cases up to 56%).[48] Using lattice parameters from The Materials Project, similar volume expansion calculations on LGPS decomposing into Li_2S, Li_3P and $Li_{15}Ge_4$ show a similar 52% expansion. [48,49] This expansion leads to mechanical fracturing LGPS in these blackened regions as it forms SEI compounds. In the uncoated sample, the majority of the surface has reacted, and the decreased ionic conductivity of these reduction products, combined with the mechanical degradation of the interface, lead to increased interfacial impedance in the degraded regions.

ALD Coated Li-Li Symmetric Cell. Before contact with Li metal, optical microscopy images of the LGPS surface showed a clean, polished surface (Figure 2a,f). EIS analysis of the ALD-coated sample immediately after cell assembly exhibits a high frequency semicircle of similar magnitude to the uncoated sample. In addition, a second, lower frequency semicircle can also be observed (Figure 1b). The higher frequency semicircle corresponds to the bulk ionic conductivity of LGPS, which demonstrates that the ALD treatment does not significantly affect the bulk electrolyte. The lower frequency semicircle is thus attributed to the Al_2O_3 film.

EIS measurements over time in the ALD coated sample show that the bulk LGPS impedance (the higher-frequency semicircle) is significantly more stable than in the uncoated sample, and it does not significantly change for the first 10 hrs. It then increases slowly over the next 100 hrs (Figure 1d). In contrast,

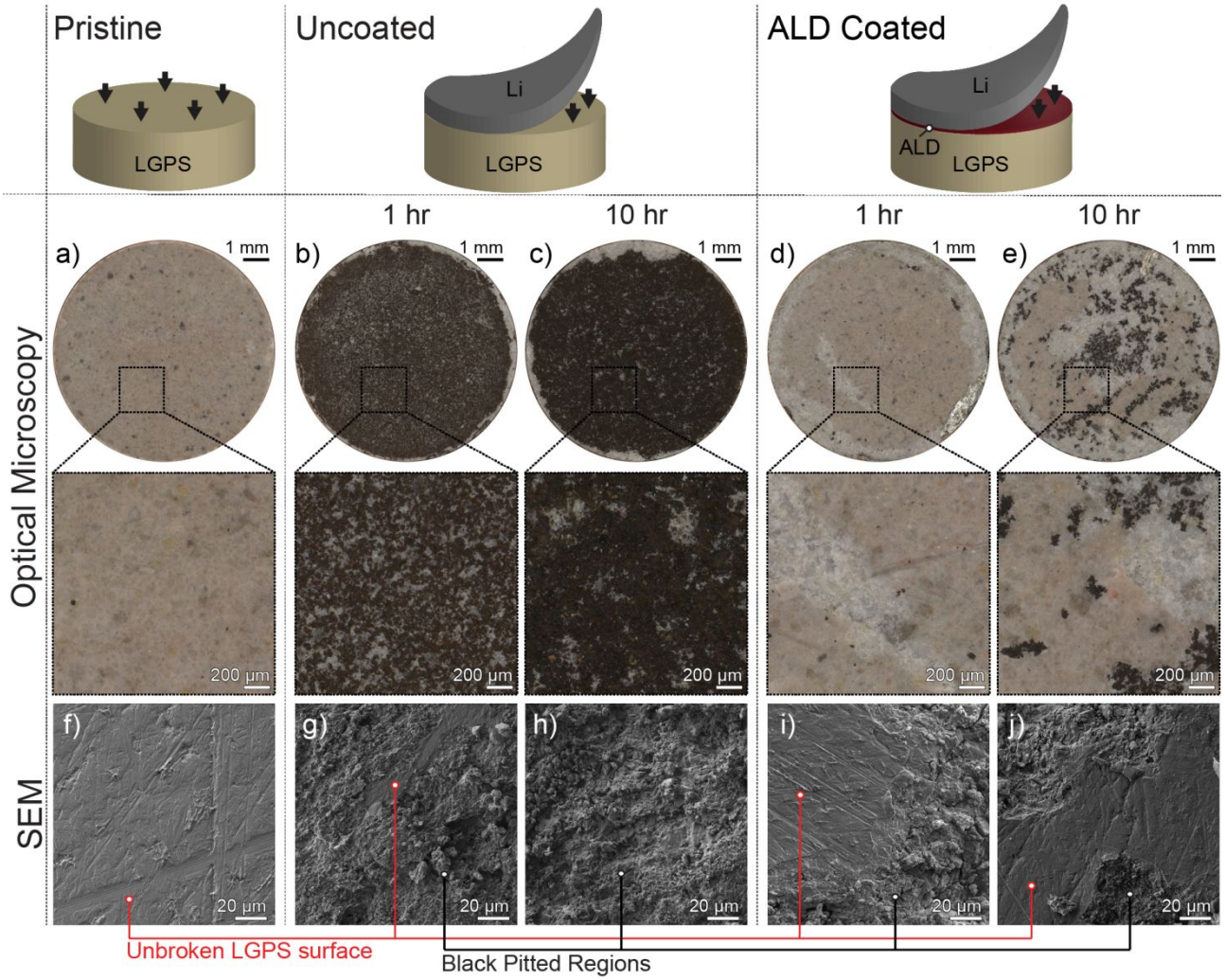

Figure 2. Optical and SEM images of the LGPS surface. (a) the LGPS surface before contact with Li metal. Images of the uncoated LGPS interface are shown after contact with Li metal for (b,g) 1 hr and (c,h) 10 hr. Images of the ALD coated LGPS surface are shown after contact with Li metal for (d,i) 1 hr and (e,j) 10 hrs. Corresponding images of the lithium surfaces that were removed from the LGPS surface for this image analysis are shown in Figure S5.

the impedance associated with the ALD layer (the lower frequency semicircle) decreases rapidly over the first 10 min. It continues to decrease slowly through the first 10 hrs, after which it begins to slowly increase over the next 100 hrs. Even after the total impedance of the ALD-coated sample begins increasing, the rate of increase remains significant slower than that of the uncoated sample and the total impedance of the uncoated sample eventually exceeds that of the ALD coated sample.

The cell cycling data (Figure 1e) further corroborate the trends observed in the EIS results. In the ALD-coated cell, a rapid drop in voltage was observed during the first several cycles, after which the voltage of the cell begins to increase. It is noteworthy that the time required for the impedance to first decrease, and then increase in the ALD-coated samples is similar for both the open-circuit and cycled cells. This implies that the reduction in impedance of the ALD film is predominantly driven by the chemical reaction with Li-metal, not by Li-ion transport through the film.

In contrast to the uncoated samples, after disassembly of the ALD-coated open circuit cells the Li remained tightly adhered to the LGPS surface. Post-mortem optical microscopy and SEM analysis were used to demonstrate the delay in surface degradation as a result of ALD treatment. After 1 hr of contact there is very little darkening of the surface (Figure 2d). After 10 hrs of contact, sparse black spots are visible, implying that LGPS degradation is beginning to occur (Figure 2e). SEM images (Figure 2 i,j) show that these black spots correspond to pitted and textured areas, similar to those seen across the entire surface of the uncoated sample. In agreement with the electrochemical data, these results demonstrate that the ALD film is able to temporarily stabilize the LGPS surface, but eventually starts to break down.

Previous computational studies have indicated that Al_2O_3 is not electrochemically stable in contact with Li metal. In particular, a recent study on potential interfacial layers for the stabilization of Li metal anodes shows a 1.23V (vs Li/Li^+) cathodic limit for pure Al_2O_3.[50] On the other hand, lithiated alumina phases (Li_xAl_yO) show significantly lower cathodic limits. Confirming these computational results, experimental studies have shown that Al_2O_3 protective layers in contact with Li-metal lithiate to form Li_xAl_yO, which has a higher ionic

This journal is © The Royal Society of Chemistry 20xx

Please do not adjust margins

conductivity than Al2O3.[31,51–53] In addition to ionic conductivity changes, both modeling and experimental methods have shown that lithiation of Al_2O_3 leads to significant volume expansion (V/V_0=2.1).[54]

In agreement with these studies, we attribute the decrease in impedance in the ALD coated samples over the first 10 hrs to the lithiation of the Al_2O_3 to form Li_xAl_yO, which has a higher ionic conductivity than Al_2O_3.[52,53] As the film expands during lithiation, it eventually begins to fracture, which allows Li metal to contact the LGPS directly. Although bypassing the ALD interlayer initially contributes to the decrease in interfacial impedance, once the Li-metal contacts the LGPS directly, the LGPS begins to locally decompose at the interface in the fracture regions. Similarly to that in the uncoated sample, the decomposition of the LGPS at the interface leads to the observed increase in interfacial impedance and the formation of localized dark spots seen in the ALD coated sample after 10 hrs of Li contact.

Operando X-ray Photoelectron Spectroscopy

The EIS and electrochemical-cycling data indicate that mechanical and chemical changes at the Li/LGPS interface evolve dynamically with time. To further probe these changes and the mechanisms behind the eventual mechanical failure of the ALD film, *operando* XPS (opXPS) was performed. In this technique, Li ions are electrochemically driven toward the SE surface allowing for real-time quantification of the chemical evolution of the SEI as it forms.[15,55]

OpXPS Overview. In opXPS, an electron gun is used to provide a flux of electrons to the surface of an exposed SE (Figure 3a). The backside of the SE is in direct contact with a Li source, and the electronically conductive Li source is grounded. Since the SE is an electronic insulator, as electronic charge accumulates on the exposed SE surface, a potential builds up across the cell. As the electrochemical potential of the exposed surface becomes more negative, Li ions are removed from the Li source and driven towards the exposed, analytical interface. At the surface, the Li ions can combine with electrons to form reduction products.

In addition to monitoring chemical changes at the interface, opXPS can also be used to analyze the total impedance and corresponding polarization associated with different cell layers.[15] During opXPS analysis, XPS measurements can be taken with and without bias (with or without electrons flooding the surface). The difference in peak position between these two measurements is equivalent to the potential difference from the grounded bottom electrode up to the phase being probed (Figure 3). For example, assume that after driving Li to the surface, the test cell had a chemical composition of LTO/LGPS/Li_2S/Li^0. If the Li_2S peak position without bias is 162.0eV and under bias the peak position shifts to 161.6eV, then the polarization across LTO/LGPS/Li_2S is 0.4eV. This hypothetical demonstrates how contributions to cell polarization can be measured up to an observed phase within the interface.

opXPS has been previously used to study the interfacial instability of Li_xP_yS (LPS).[15] It was demonstrated that the LPS decomposes into Li_2S, Li_3P and Li_2O before Li^+ can be reduced to form Li metal. For the reader's reference, a more comprehensive explanation of the details and physics of opXPS is also included in that study.[15]

OpXPS Polarization Measurements. In this study, opXPS was used to quantify the chemical evolution of the LGPS/Li-metal

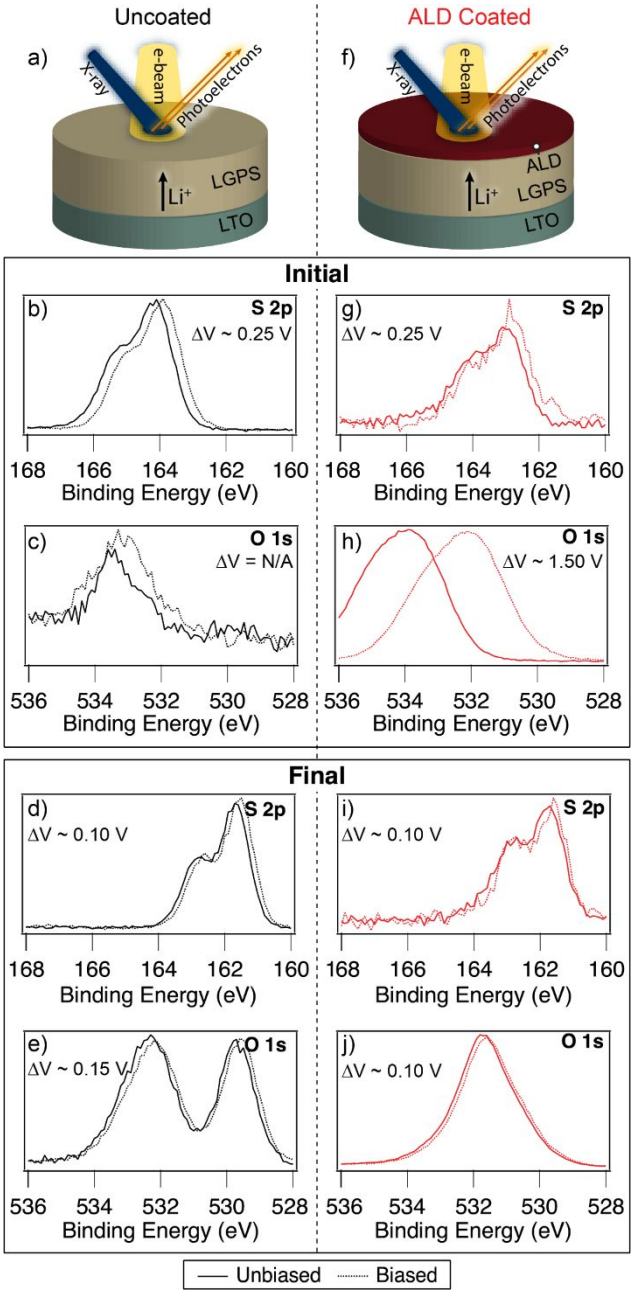

Figure 3. Comparison of XPS measurements for uncoated (black) and ALD coated (red) LTO/LGPS anode-free cells. (a,f) Schematic showing uncoated and ALD coated anode-free cells. XPS spectra of the S 2p and O 1s peaks were acquired with and without bias at t = 0 hrs (initial) and t = 12 hrs (final). The S 2p spectra at t = 0 hrs (b,g) and t = 12 hrs (d,i) correspond to LGPS and Li_2S respectively. The O 1s spectra in the ALD coated sample at t = 0 hrs (h) and t = 12 hrs (j) correspond to the Al_2O_3 film and Li_xAl_yO layer respectively. The O 1s spectra in the uncoated sample at (c,e) correspond to impurities.

interface, with and without ALD interlayers. Anode-free cells were fabricated using a composite $Li_4Ti_5O_{12}$ electrode (LTO) as the Li source. LTO was chosen because it has a relatively flat voltage profile, and the fact that the LGPS/LTO interface is more stable than Li/LGPS (Figure S4b). The use of LTO therefore minimized changes in cell polarization associated with the bottom electrode/LGPS interface. For the ALD coated samples, a thinner (4 nm) coating was used so that the underlying LGPS spectra could simultaneously be observed.

For XPS analysis, the bare LGPS surface of the uncoated sample (Figure 3a) and the Al_2O_3 surface of the ALD-coated sample (Figure 3f) were exposed to an ultra-high vacuum (UHV) environment. A bias was applied for 12 hrs, which drove Li ions to the exposed surface. The cell polarization was measured at the start and end of the 12-hr lithiation. In this experiment, four different experimental conditions were measured for each sample, (I) before lithiation non-biased, (II) before lithiation biased, (III) after lithiation non-biased, (IV) after lithiation biased. For the control sample, Figure 3b shows the S 2p core spectrum under conditions I (solid line) and II (dashed line) while Figure 3g shows the S 2p under conditions III (solid line) and IV (dashed line).

Consistent with the EIS results from the Li-Li symmetric cells, the uncoated sample exhibits only a small shift in the S spectra with and without bias (0.25V, Figure 3b). Since the sulfur at this point is only associated with the LGPS phase, this shift corresponds to the polarization across the LTO/LGPS stack. The ALD-coated sample shows an equivalently small shift in the S spectra (Figure 3g). This equivalent shift demonstrates that the polarization across the LTO/LGPS portions of the test cells were nearly identical, regardless of the presence of an ALD coating. These results are consistent with the EIS data shown in Figure 1b, where the high-frequency semi-circle associated with bulk transport through the LGPS is similar in both the coated and uncoated samples.

However, unlike the uncoated sample, the ALD coated sample exhibits a large shift in the O spectrum (~1.5V) under bias, which corresponds to polarization across the entire LTO/LGPS/Al_2O_3 stack (Figure 3h). Since ionic transport through the LTO/LGPS portion of the stack contributed ~0.25V to the cell polarization, the contribution to polarization associated with the initial Al_2O_3 layer was ~1.25 V. However, the difference between the biased and unbiased spectra decreased rapidly during lithiation. After 12 hrs, the contributions to polarization associated with the Al 2p and O 1s (i.e. the initial ALD layer) were negligible (~0.1 V or less) (Figure 3j). These results agree well with the EIS and voltage trace data shown in Figure 1, which exhibited an initial decrease in impedance.

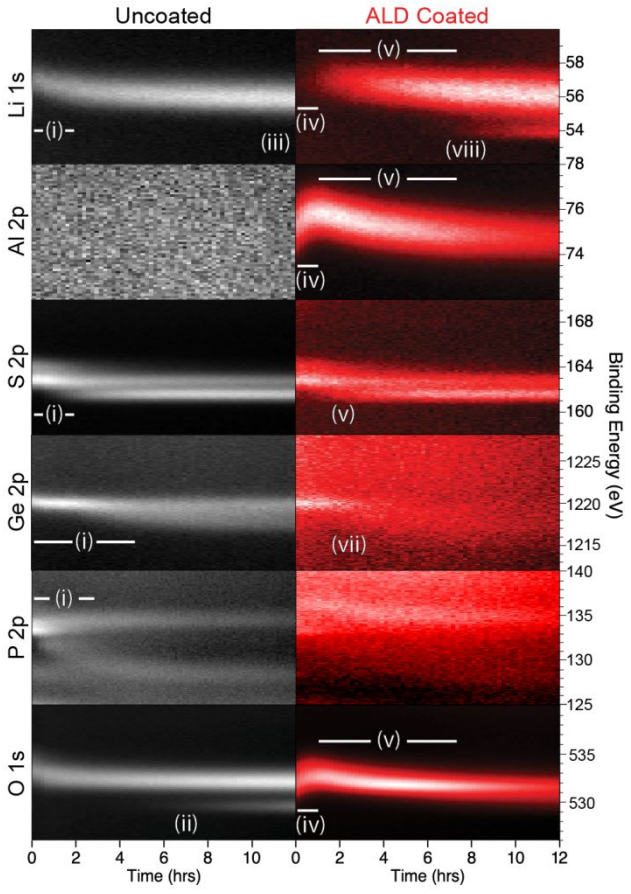

Figure 4. Spectra from opXPS at the LPGS surface for the Li 1s, Al 2p, S 2p, Ge 2p, P 2p, and O 1s peaks. Data is plotted such that spectra of high intensity appear white.

OpXPS Chemical Evolution Measurements. In addition to polarization measurements, opXPS was used to probe the time-dependent chemical evolution of the surface. Throughout the 12 hr lithiation of the coated and uncoated samples, XPS spectra (Li 1s, Al 2p, S 2p, C 1s, O 1s, and Ge 2p core levels) were acquired every 15 min. Spectra were taken while the bias was applied. The evolution of these XPS spectra is shown in Video A, and a graphical representation is shown in Figure 4. In the graphical representations, each image represents one core level for a specific sample (uncoated: grey, ALD coated: red), with areas of high intensity appearing white and areas of low intensity appearing black. Analysis of both Figure 4 and Video A reveal significant differences in the chemical evolution of the SEI layer between the two samples as Li is transported to the surface. An schematic summarizing the observed changes is given in Figure 6.

For the uncoated sample, S, P and Ge at the surface are quickly reduced to Li_2S, Li_xP and reduced Ge. These changes are clearly observed in the S 2p, P 2p, and Ge 2p core levels, but also evident in the Li 1s core spectra, which exhibit a consistent and gradual shift toward lower binding energy. (Figure 4(i)) These reduction products match those expected based on previous computational and experimental studies.[12,22,23] After approximately 6-8 hrs, a low-binding-energy peak associated with Li_2O begins to appear (Figure 4 (ii)). Previous opXPS results on LPS show that this Li_2O formation originates from oxygen impurities in the solid electrolyte.[15] Even after 12 hrs of charging, no metallic Li was present at the surface of the uncoated sample (Figure 4 (iii)).

For the ALD-coated sample, the initial Al_2O_3 coating attenuated the signal from Ge and P, and significantly reduced the signal associated with S. During the initial lithiation of this sample, the most significant chemical changes were observed in the Al 2p and O 1s core levels. As seen in Figure 4(iv), during

This journal is © The Royal Society of Chemistry 20xx

Please do not adjust margins

the first hour of lithiation the binding energies associated with the Al 2p and O 1s peaks increase; and for the Li 1s spectra very little Li was observed. After one hour, a more pronounced Li signal was observed and the Li 1s, Al 2p and O 1s core levels experienced a notable decrease in binding energy (Figure 4(v)). At around 2 hours a shift in the S peaks occurs, indicating some reduction of S into Li_2S on the LGPS surface (Figure 4(vi)). Although greatly attenuated, a shift is also faintly visible in the Ge 2p peak indicating the reduction of germanium (Figure 4(vii)). At the 6 hour point a new low binding energy peak associated with Li metal appears (Figure 4(viii)). These observations from figure 4 indicated two things. First, the contribution to polarization associated with the ALD layer decrease dramatically during the first hour, which is evident by the increasing binding energy position (Figure 4(iv)). Second, the ALD layer continues to chemically evolve during prolonged lithiation, which is evidenced by the decrease in binding energy after one hour of lithiation to form Li_xAl_yO (Figure 4(v)).

To provide further mechanistic insight into the evolution occurring at the ALD interface, AES analysis was also performed after the 12-hour opXPS lithiation (Figure 5). These results indicate that cracks formed in the ALD layer, which lead to preferential localized Li deposition within the cracks.

By combining the insights from the opXPS observations with the AES observations, we propose the following mechanism. During the initial lithiation of Al_2O_3, Li_xAl_yO begins to form, which causes an increase in ionic conductivity of the ALD film as it lithiates (Figure 6b). This increase in ionic conductivity results

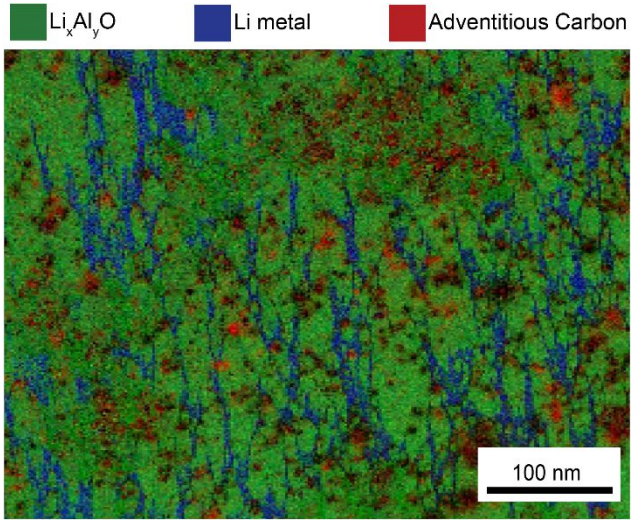

Figure 6. AES spectrograph of ALD coated LGPS surface after opXPS experiments. The lithiated ALD film has cracked and Li metal has plated in the cracks.

in a subsequent shift of spectral intensity toward higher binding energy in the opXPS measurements. However, the formation of Li_xAl_yO leads to cracking, as seen in the AES data, due to the volumetric expansion of the Al_2O_3 film as it reacts with lithium[51].The formation of these cracks likely coincide with appearance of Li_2S, which is an initial reduction component of LGPS reacting with Li. After 6 hrs, Li metal begins to appear within the cracks (Figure 6b). In contrast, Li plating was not

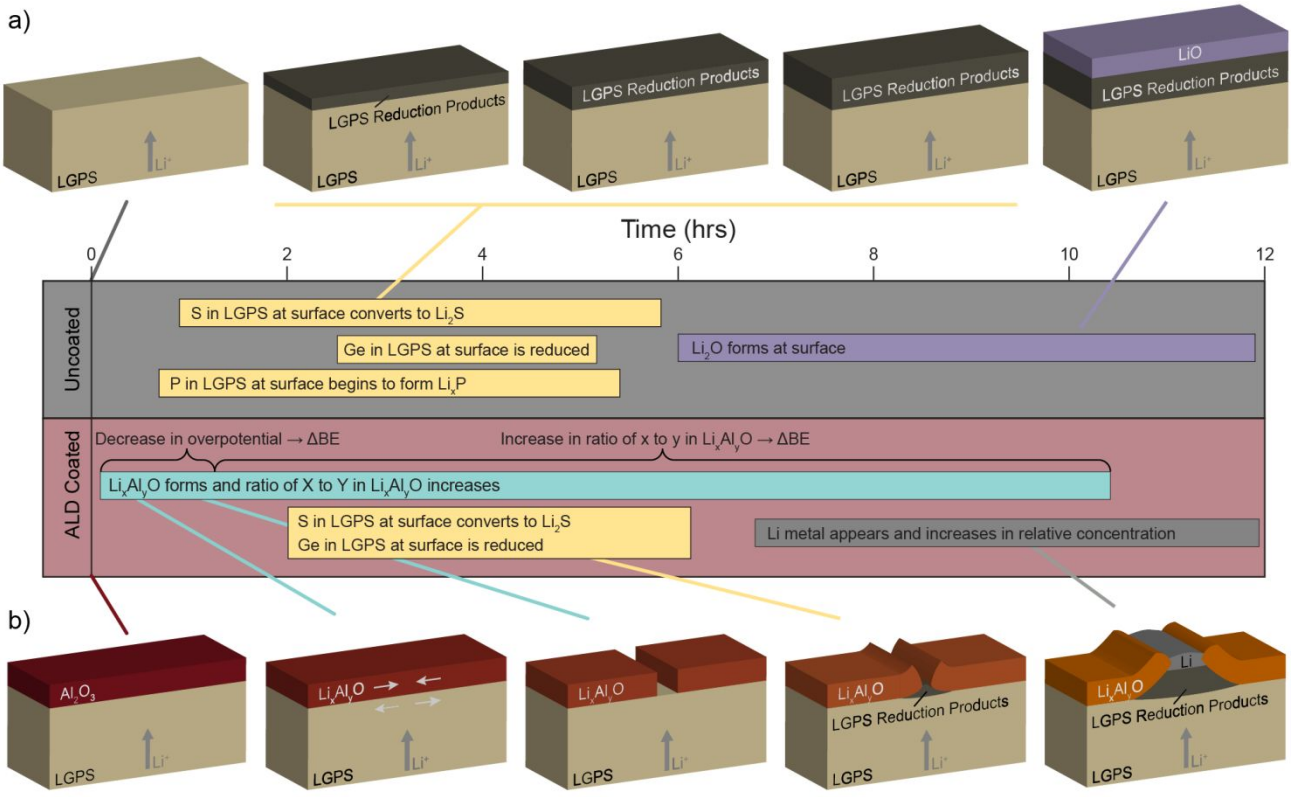

Figure 5. Timeline and schematics showing evolution of the LGPS surface during opXPS experiments. (a) The Uncoated sample shows rapid reduction of the LGPS into Li_2S, Li_xP and Li_xGe. After ~6 hr, Li_2O begins forming at the surface. Li metal plating is not observed even after 12 hr. (b) The ALD coated sample shows the lithiation of the Al_2O_3 layer into Li_xAl_yO which leads to cracking of the ALD film. As the cracking occurs, the LGPS begins to be reduced and by ~7 hr Li metal begins plating out in the cracks. ΔBE is the change in binding energy observed in the XPS spectra.

detected throughout the entire 12 hr experiment in the uncoated sample. This difference indicates that despite the mechanical fracturing of the Al_2O_3 film, the ALD coating limits the reduction of LGPS and corresponding SEI formation, allowing for Li plating to occur after less charge has been passed.

Operando optical visualization

To provide further insights into the coupled electro-chemo-mechanical behavior of these systems, *operando* optical video microscopy was performed during electrochemical cycling.[56,57] This *operando* visualization technique was performed in an LTO/LGPS/Mo cell, where 300 nm thick molybdenum current collectors were sputtered onto the ALD-coated (Figure 7b) and uncoated (Figure 7a) LGPS surfaces to form LTO/LGPS/Mo anode-free cells.[58] Mo deposition was performed in an argon-glovebox-integrated sputter chamber, without any air exposure. A galvanostatic current was applied to drive Li from the LTO electrode to the surface of the Mo current collector. A current density of 0.01 mA/cm^2 across the Mo current collector was used in order to approximate the currents used in the opXPS experiments.

The initial surfaces of the current collectors deposited on both the ALD-coated and uncoated samples are shown Figure 7e,f. The synchronized evolution of the Mo surfaces and cell voltage traces are shown in Videos B and C.

Operando optical microscopy images of the uncoated sample after 10 hrs of charging exhibit a relatively homogenous darkening of the Mo current collector (Video B, Figure 7g). This darkening also extends radially beyond the edges of the circle and is attributed to reduction of the LGPS and formation of SEI byproducts beneath the current collector. In contrast, in the ALD-coated sample, this homogeneous darkening and radial expansion are not observed. Instead, evidence of Li plating "hotspots" appears across the surface of the current collector (Video C, Figure 7h). These nucleation events occur in the early stages of plating (<2 hr).

Ex situ SEM images of focused ion beam cross sections (FIB-SEM) in Figure 7c,d,i-k show the surface before and after charging. In the uncoated sample, a clean LGPS/Mo interface is observed before charging. After charging, LGPS reduction products are visible along the entire Mo/LGPS interface (Figure 7i).

In the ALD-coated sample, the thin Al_2O_3 layer is visible between the LGPS and Mo before charging (Figure 7d). After charging, distinct differences were seen in the sub-surface morphology between regions in the vicinity of a hotspot and the regions where no optically visible changes occurred. In the FIB-SEM images, the majority of the interface in regions away from hotspots showed no evidence of LGPS reduction products (Figure 7j). In sub-surface regions adjacent to the hotspots, clear evidence of LGPS reduction products and Li plating were visible.

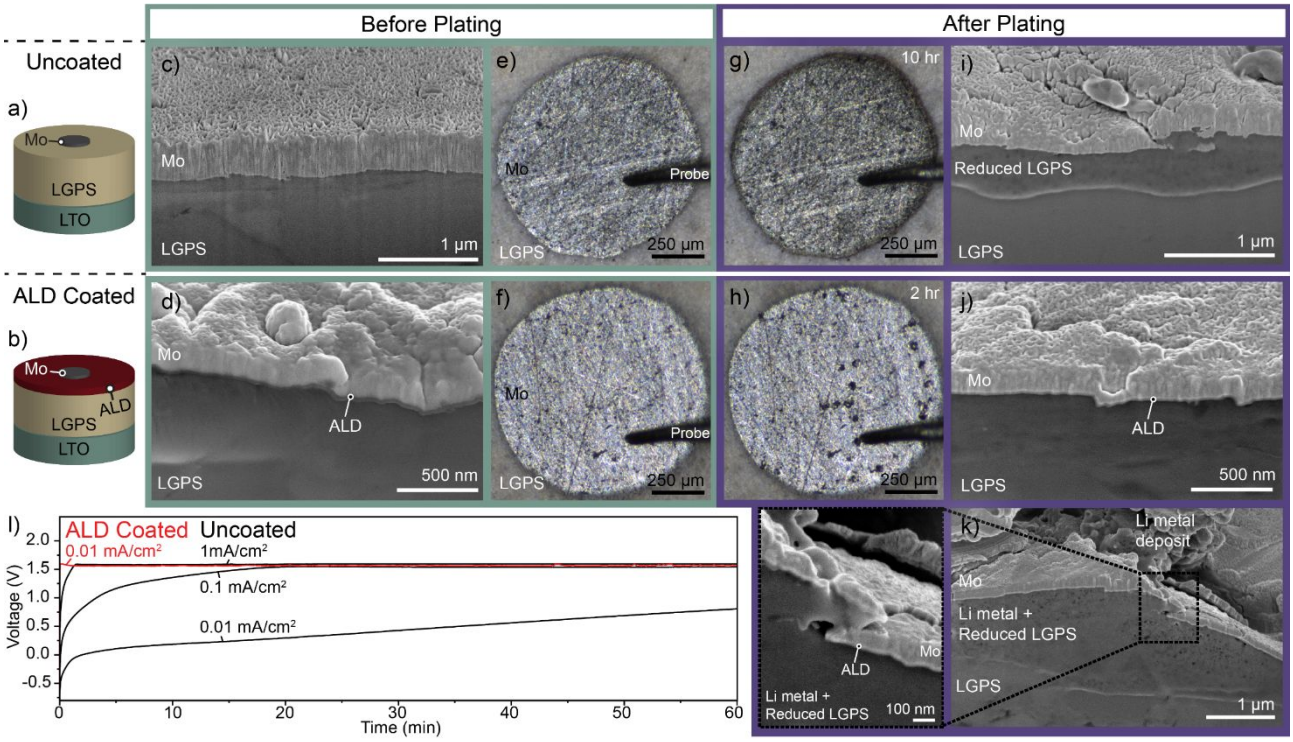

Figure 7. *Operando* optical microscopy of LTO/LGPS/Mo anode-free cells. (a) and (b) show schematics of the anode-free cells in the uncoated and ALD coated cases respectively. (e,f) Before charging in both the uncoated and ALD coated samples, the circular Mo current collector is visible on the surface of the LGPS. (c,d) FIB-SEM cross-sectional images show clean interfaces between the Mo and the LGPS, with the ALD film visible at the interface of the ALD coated sample. (g) In the uncoated sample, after 10 hr charging at 0.01 mA/cm^2 visible darkening occurs across the surface of the current collector as the LGPS under the Mo is reduced. (i) After charging, cross-sectional FIB-SEM confirms reduction across the entire LGPS/Mo interface. (h) In contrast, after only 2 hrs of charging at 0.01 mA/cm^2, the ALD coated sample shows Li metal deposition in several hotspots with other regions of the ALD sample showing no visible LGPS reduction. (j) Cross-sectional FIB-SEM confirms that away from hotspots there is little evidence of LGPS reduction or Li metal plating. (i) Cross-sectional FIB-SEM at the hotspots shows Li metal and reduced LGPS underneath cracks in the Mo. Additional Li-metal is visible on the surface after having extruded through cracks in the ALD/Mo bilayer. (l) Voltage profile of LTO/LGPS/Mo anode-free cells at varying current densities.

This journal is © The Royal Society of Chemistry 20xx

Please do not adjust margins

Additionally, while the ALD film remains adhered to the Mo surface, cracking of the ALD and Mo films can be observed. Furthermore, the base of the Li-metal deposit, which extruded through the cracks, is visible as well (Figure 7k). This observation is consistent with the AES analysis, where lithium plating is selectively observed in the regions where the ALD film cracked. The extruded geometry of the plated Li metal is further evidence of the coupled mechanical-electrochemical nature of the interfacial dynamics, as the flow of Li out of the crack will be affected by visco-plastic nature of Li metal.[47]

We note that the spacing between the cracks from the AES result were much smaller than the spacing between the macroscopic Li filaments grown in the optical visualization platform. This difference in spacing could be due to several factors, including the mechanical constraint of the metal current collector on top of the ALD film (which is absent in the AES analysis), the electrical conductivity of the metal current collector, variations in the local electric field, etc. While a full electro-chemo-mechanical analysis would be needed to fully reconcile these two experimental platforms, these results demonstrate the critical role that mechanical stress evolution plays at Li-metal/SE interfaces, and points towards the need for development of mechanically tough and ionically conductive interlayers.

One of the major advantages of the *operando* visualization platform is the ability to time-synchronize the voltage trace of the cell with the optical images. The corresponding voltage traces from the *operando* cell are shown in Figure 7l. In the ALD-coated sample, the cell voltage rises to 1.53 V within the first few seconds at a current density of 0.01 mA/cm^2. This voltage corresponds to the measured open-circuit voltage of the LTO electrode vs Li metal in a liquid electrolyte (Figure S8) and indicates that Li metal is depositing at the anode.

In contrast, the voltage trace of the uncoated sample at 0.01 mA/cm^2 slowly rises without reaching the Li metal/LTO potential even after 23 hrs (Figure S9). Not reaching this potential implies that LGPS is being continually reduced at the interface, and Li metal has not yet plated out. This result is consistent with the FIB-SEM observation of the uncoated sample where no Li-plating is observed and a reduced LGPS SEI layer is present along the interface (Figure 7i). This result is also consistent with the opXPS results, wherein the LGPS surface decomposes before metallic Li forms, and the onset of Li metal plating occurs sooner in the ALD-coated sample.

By going to higher current densities in the uncoated sample, the onset of Li metal plating can be accelerated dramatically, as shown by the time required to reach the plateau voltage of 1.53 (Figure 7l). Interestingly, the amount of charge required to reach 1.53 V decreases as current density increases. In other words, if the current density is increased by a factor of 10, the time required for the onset of Li plating decreases by more than a factor of 10.

One way to rationalize this behavior is to consider the competing kinetics of Li-plating and LGPS reduction. As the total flux of Li ions to the electrochemically active interface increases, a kinetic competition between reaction pathways determines the relative rate of each reaction. At low current densities in the uncoated sample, the LGPS is reduced as quickly as Li^+ are transported to the surface, but at higher current densities the flux of Li^+ outpaces the reduction of the LGPS and Li metal begins to plate on the surface. These different pathways are analogous to spatially varying kinetics among different reaction pathways at Li metal/liquid electrolyte interfaces, which have been shown to strongly influence the voltage trace of Li metal batteries.[57,59,60]

The disproportional hastening of lithium plating at higher current densities in the uncoated samples also points towards one of the influences that the ALD film has on SEI formation. In the ALD-coated sample, the local current density within the cracks is significantly amplified, and therefore the onset of Li plating occurs much sooner than in the uncoated samples. This hastening influences the nature of the SEI that forms. For example, as shown in the opXPS analysis, Li_2O forms after extensive SEI formation in the uncoated sample, which was not observed in the ALD coated sample before metallic Li plated out.

As shown in Figures 1-2, the evolution of the interfacial impedance of the cell and stabilization of cycling behavior is influenced by the ALD film even after degradation begins to occur, which is likely due to the nature and extent of LGPS reduction at the interface. Ultimately, the design of a stable interlayer must take into account the coupled electro-chemo-mechanical evolution of the interface. Through an improved understanding of the dynamic evolution of the interface with and without the presence of artificial SEI layers, the insights provided from this study point towards design principles for further improvement of interlayers.

Conclusions

In summary, we applied a multi-modal approach to understand LGPS degradation in solid-state Li-metal batteries, and the impact of ALD Al_2O_3 interlayers on this interface. We show that Al_2O_3 interlayers provide short-term stabilization of the interface and slow down the eventual SEI formation. We utilized these interlayers as a model system to improve our understanding of the mechanisms behind SE stabilization and the electro-chemo-mechanical phenomena that lead to eventual decay of artificial SEIs.

As-deposited Al_2O_3 has low ionic conductivity, which increases due to lithiation to form Li_xAl_yO. This lithiation process also leads to volumetric expansion of the ALD film. Due to the brittle nature of Al_2O_3 it is unable to accommodate this strain and eventually fractures. As a consequence of interlayer cracking, current focusing within the cracks occurs, which accelerates Li metal plating relative to SEI formation.

We observed two main effects that limit the long-term effectiveness of Al_2O_3 and similar artificial SEI. 1. During early stage cycling the low ionic conductivity of Al_2O_3 increases the overall cell impedance. This challenge can be directly addressed by developing interlayers with higher ionic conductivities. 2. With extended cycling the ALD layer fractures and is no longer able to passivate the LGPS surface. The Al_2O_3 coatings break down through a two-step process. Initially, the reaction with

lithium metal results in the formation of Li_xAl_yO, which is desirable, and increases the ionic conductivity of the artificial SEI. However, after continued lithiation of the ALD film, volumetric expansion leads to cracking. By either entirely preventing the lithiation of the artificial SEI and/or by modifying the mechanical properties of the artificial SEI, its cracking and eventual degradation may be prevented.

To summarize, if ALD interlayers can be developed with 1. high ionic conductivities, 2. minimal volume changes when in contact with Li metal, and 3. improved mechanical properties, long term-improvement in interface stability and performance may be realized.

Experimental Section

Preparation of LGPS State Electrolyte

All air-sensitive materials were handled in an Ar-filled glovebox (MBraun) with oxygen and moisture levels maintained < 0.5 ppm. $Li_{10}GeP_2S_{12}$ (LGPS) powder (MSE Supplies) was used as received. 6 mm diameter pellets were fabricated from 106 mg of LGPS powder by cold pressing (26 °C) at 520 MPa for 10 min. After pressing, both sides of the pellets were polished using 2000 grit sandpaper. Sample densities were determined using geometrical measurements and weight. Thicknesses were consistently 1.98-2.03 mm. Relative densities compared to that of theoretical LGPS were consistently 89%-90%.

Li-Li Symmetric Cell Assembly

Li metal electrodes were prepared from metal foil (750 µm thick, Alfa Aesar). The Li foil surface was scraped and flattened to remove surface layers and achieve a shiny metallic surface. Symmetric Li/LGPS/Li cells were then assembled with 8.8 MPa stack pressure.

LTO Pre-lithiation

Li-LTO coin cells were assembled and cycled to lithiate the LTO active material. Li-LTO cells were assembled using CR2032 coin cell cases, spacers, and wave springs. The electrolyte was 1M $LiPF_6$ in 1:1 EC:EMC (Soulbrain) and 75 µL was used per cell. Li metal (750 µm thick, Alfa Aesar) was used as the counter/reference electrode against the LTO working electrode. The LTO anodes were received from the CAMP facility at Argonne National Laboratory and have a capacity of 160 mAh/g and a loading of 1.96 mAh/cm^2.

After assembly, cells were first rested for 6 hrs to ensure full electrolyte infiltration into the LTO anodes, followed by 3 formation cycles at C/10 rate between 1-2 V vs. Li counter electrodes. For the last formation cycle, cells were stopped after once a cutoff voltage of 1.53 V was reached, which is just before the end of the LTO voltage plateau (Figure S8). The lithiated LTO electrodes were collected from coin cells and rinsed with fresh dimethyl carbonate multiple times to remove electrolyte residue. The electrodes were dried in the glovebox antechamber under vacuum.

LTO Anode-free Cell Assembly

Lithiated LTO, LGPS powder, and carbon black conductive additive (C-nergy Super C65) were combined in a 3:6:1 (wt%) ratio and mixed by mortar and pestle for 10 min to form a composite LTO electrode. LTO/LGPS anode-free cells were formed by lightly pressing and electrolyte pellet using 104 mg LGPS powder, and then subsequently pressing an additional 7.3 mg (1 mAh/cm^2) composite LTO powder against one side of the electrolyte. The entire anode-free cell was then pressed at 520 MPa for 10 min. The LGPS surface was polished with 2000 grit sandpaper. 300 nm current collectors were sputtered onto the surface of the samples used for *operando* video microscopy using a glovebox integrated Angstrom Engineering Nexdep sputter coater.

ALD Al_2O_3 Surface Coating of LGPS Pellets

ALD coatings were carried out in a Savannah S200 Ultratech ALD reactor that is integrated into an argon glovebox, allowing for direct coating of the LGPS surface and cell assembly without air exposure.[31] Trimethylaluminum (TMA) and O_3 as precursors. LGPS pellets were coated at 60°C using TMA pulses of 0.1 s, ozone pulses of 4 s, and a carrier gas flow rate of 10 SCCM Argon. Growth rates were measured on (100) silicon using both *in situ* QCM and ex-situ ellipsometry. Al_2O_3 growth rates of 1 Å/cycle were measured using SEM (Figure S2, FEI Helios 650 Nanolab SEM/FIB) and ellipsometry (Woollam M-2000DI). Multiple ALD thicknesses were tested and 200x (20 nm) was chosen based on preliminary performance for Li-Li symmetric cells and for operando video microscopy cells (Figure S10). A thinner (4 nm) coating was used for the opXPS experiments so that the underlying LGPS spectra could simultaneously be observed.

Electrochemical Characterization

All electrochemical measurements were taken using biologic potentiostats (SP-200 and VSP) at 26 °C. Complex impedance measurements were taken using EIS with a 10-mV sinus amplitude and a frequency range of 6 MHz to 1 kHz. Li-Li symmetric cell cycling was performed at 0.1 mA/cm^2. Lithium plating in LTO/LGPS anode-free cells for *operando* XPS was done at ~4 µA/cm^2. Anode-free cells with currents between 0.01 mA/cm^2 – 1 mA/cm^2 were used for *operando* optical visualization.

SEM and Optical Microscopy

Post-mortem optical microscope images of the interface were taken in an Ar environment using a Keyence VHX-7000 digital microscope. A Tescan MIRA3 GMU FEGSEM was used for top-down SEM analysis. FIB cross-sections were made and analyzed using an FEI Helios Nanolab 650 SEM/FIB.

Optical Visualization Cell

Synchronized plan-view optical visualization was performed using a custom build visualization platform. Current was applied by a probe contacting the Mo surface. Videos were taken with an Opto Engineering RT-HR-6M-71 telecentric lens.

This journal is © The Royal Society of Chemistry 20xx

Please do not adjust margins

Operand Photoelectron Spectroscopy (op-XPS)

OpXPS measurements were performed using a Physical Electronics 5600 photoelectron spectrometer at ultrahigh vacuum (~5 × 10^{-10} Torr). Monochromated Al Kα X-rays were generated with an anode power of 350 W. The sample surface normal was oriented at 45° to both the X-ray source and photoelectron spectrometer. An optimal noise to resolution pass energy was determined to be 29.35 eV. In this work relative (delta) Binding-energy (BE) shifts are used as described elsewhere.[55] Curve fitting and data processing was performed using Igor Pro with a custom program adapted from Schmid et. al.[61]

Auger Electron Spectroscopy

AES measurements were performed using a Physical Electronics 670 system, under beam energy of 5 kV, with 20-nA beam current. Typical pressures were ~7 × 10^{-10} Torr. Samples were loaded into the XPS without air exposure through a connected glovebox. After *operando* XPS testing samples were transferred directly into AES for analysis through a UHV connection.

Conflicts of interest

There are no conflicts to declare

Acknowledgements

This research was supported by a Bosch Energy Research Network (BERN) grant. The authors acknowledge the University of Michigan College of Engineering for financial support and the Michigan Center for Materials Characterization for use of the instruments and staff assistance. This work was authored in part by the National Renewable Energy Laboratory, operated by Alliance for Sustainable Energy, LLC, for the U.S. Department of Energy (DOE) under Contract No. DE-AC36-08GO28308. Funding provided by the Laboratory Directed Research and Development program. The views expressed in the article do not necessarily represent the views of the DOE or the U.S. Government. A. L. D. acknowledges that this material is based upon work supported by a National Science Foundation Graduate Research Fellowship under Grant No. (DGE 1256260). The authors would also like to thank the U.S. Department of Energy Cell Analysis, Modeling, and Prototyping (CAMP) Facility of Argonne's Chemical Sciences and Engineering Division for providing the electrode materials.

Notes and references

1 Z. Zhang, Y. Shao, B. Lotsch, Y. S. Hu, H. Li, J. Janek, L. F. Nazar, C. W. Nan, J. Maier, M. Armand and L. Chen, *Energy Environ. Sci.*, 2018, **11**, 1945–1976.

2 Z. Gao, H. Sun, L. Fu, F. Ye, Y. Zhang, W. Luo and Y. Huang, *Adv. Mater.*, 2018, **30**, 1705702.

3 N. J. Taylor, S. Stangeland-Molo, C. G. Haslam, A. Sharafi, T. Thompson, M. Wang, R. Garcia-Mendez and J. Sakamoto, *J. Power Sources*, 2018, **396**, 314–318.

4 N. J. Dudney, *Mater. Sci. Eng. B*, 2005, **116**, 245–249.

5 N. Kamaya, K. Homma, Y. Yamakawa, M. Hirayama, R. Kanno, M. Yonemura, T. Kamiyama, Y. Kato, S. Hama, K. Kawamoto and A. Mitsui, *Nat. Mater.*, 2011, **10**, 682–686.

6 Y. Seino, T. Ota, K. Takada, A. Hayashi and M. Tatsumisago, *Energy Environ. Sci.*, 2014, **7**, 627–631.

7 S. Chen, D. Xie, G. Liu, J. P. Mwizerwa, Q. Zhang, Y. Zhao, X. Xu and X. Yao, *Energy Storage Mater.*, 2018, **14**, 58–74.

8 K. H. Park, Q. Bai, D. H. Kim, D. Y. Oh, Y. Zhu, Y. Mo and Y. S. Jung, *Adv. Energy Mater.*, 2018, **8**, 1800035.

9 Y. Kato, S. Hori, T. Saito, K. Suzuki, M. Hirayama, A. Mitsui, M. Yonemura, H. Iba and R. Kanno, *Nat. Energy*, 2016, **1**, 16030.

10 A. Sakuda, A. Hayashi and M. Tatsumisago, *Sci. Rep.*, 2013, **3**, 2261.

11 F. Han, Y. Zhu, X. He, Y. Mo and C. Wang, *Adv. Energy Mater.*, 2016, **6**, 1501590.

12 Y. Zhu, X. He and Y. Mo, *J. Mater. Chem. A*, 2016, **4**, 3253–3266.

13 W. D. Richards, L. J. Miara, Y. Wang, J. C. Kim and G. Ceder, *Chem. Mater.*, 2016, **28**, 266–273.

14 B. Wu, S. Wang, W. J. Evans IV, D. Z. Deng, J. Yang and J. Xiao, *J. Mater. Chem. A*, 2016, **4**, 15266–15280.

15 K. N. Wood, K. X. Steirer, S. E. Hafner, C. Ban, S. Santhanagopalan, S.-H. Lee and G. Teeter, *Nat. Commun.*, 2018, **9**, 2490.

16 L. Sang, R. T. Haasch, A. A. Gewirth and R. G. Nuzzo, *Chem. Mater.*, 2017, **29**, 3029–3037.

17 L. E. Camacho-Forero and P. B. Balbuena, *J. Power Sources*, 2018, **396**, 782–790.

18 B. Chen, J. Ju, J. Ma, J. Zhang, R. Xiao, G. Cui and L. Chen, *Phys. Chem. Chem. Phys.*, 2017, **19**, 31436–31442.

19 P. Bron, B. Roling and S. Dehnen, *J. Power Sources*, 2017, **352**, 127–134.

20 Y. Zhu, X. He and Y. Mo, *ACS Appl. Mater. Interfaces*, 2015, **7**, 23685–23693.

21 S. Wenzel, D. A. Weber, T. Leichtweiss, M. R. Busche, J. Sann and J. Janek, *Solid State Ionics*, 2016, **286**, 24–33.

22 S. Wenzel, S. Randau, T. Leichtweiß, D. A. Weber, J. Sann, W. G. Zeier and J. J. Janek, *Chem. Mater.*, 2016, **28**, 2400–2407.

23 M. Sakuma, K. Suzuki, M. Hirayama and R. Kanno, *Solid State Ionics*, 2016, **285**, 101–105.

24 Y. Mo, S. P. Ong and G. Ceder, in *Chemistry of Materials*, 2012, vol. 24, pp. 15–17.

25 C. Ma, Y. Cheng, K. Yin, J. Luo, A. Sharafi, J. Sakamoto, J. Li, K. L. More, N. J. Dudney and M. Chi, *Nano Lett.*, 2016, **16**, 7030–7036.

26 Z. Zhang, S. Chen, J. Yang, J. Wang, L. Yao, X. Yao, P. Cui and X. Xu, *ACS Appl. Mater. Interfaces*, 2018, **10**, 2556–2565.

27 E. Umeshbabu, B. Zheng, J. Zhu, H. Wang, Y. Li and Y. Yang, *ACS Appl. Mater. Interfaces*, 2019, **11**, 18436–18447.

28 C. Wang, K. R. Adair, J. Liang, X. Li, Y. Sun, X. Li, J. Wang, Q. Sun, F. Zhao, X. Lin, R. Li, H. Huang, L. Zhang, R. Yang, S. Lu

and X. Sun, *Adv. Funct. Mater.*, 2019, **29**, 1900392.
29 Y. Gao, D. Wang, Y. C. Li, Z. Yu, T. E. Mallouk and D. Wang, *Angew. Chemie Int. Ed.*, 2018, **57**, 13608–13612.
30 P.-H. Chien, X. Feng, M. Tang, J. T. Rosenberg, S. O'Neill, J. Zheng, S. C. Grant and Y.-Y. Hu, *J. Phys. Chem. Lett.*, 2018, **9**, 1990–1998.
31 E. Kazyak, K. N. Wood and N. P. Dasgupta, *Chem. Mater.*, 2015, **27**, 6457–6462.
32 Y. Cao, X. Meng and J. W. Elam, *ChemElectroChem*, 2016, **3**, 858–863.
33 J. Liu and X. Sun, *Nanotechnology*, 2015, **26**, 024001.
34 X. Meng, X.-Q. Yang and X. Sun, *Adv. Mater.*, 2012, **24**, 3589–3615.
35 C.-F. Lin, A. C. Kozen, M. Noked, C. Liu and G. W. Rubloff, *Adv. Mater. Interfaces*, 2016, **3**, 1600426.
36 X. Han, Y. Gong, K. Fu, X. He, G. T. Hitz, J. Dai, A. Pearse, B. Liu, H. Wang, G. Rubloff, Y. Mo, V. Thangadurai, E. D. Wachsman and L. Hu, *Nat. Mater.*, 2017, **16**, 572–579.
37 N. P. Dasgupta, H.-B.-R. Lee, S. F. Bent and P. S. Weiss, *Chem. Mater.*, 2016, **28**, 1943–1947.
38 S. M. George, *Chem. Rev.*, 2010, **110**, 111–131.
39 J. W. Elam, N. P. Dasgupta and F. B. Prinz, *MRS Bull.*, 2011, **36**, 899–906.
40 L. Chen, J. G. Connell, A. Nie, Z. Huang, K. R. Zavadil, K. C. Klavetter, Y. Yuan, S. Sharifi-Asl, R. Shahbazian-Yassar, J. A. Libera, A. U. Mane and J. W. Elam, *J. Mater. Chem. A*, 2017, **5**, 12297–12309.
41 S. Neudeck, A. Mazilkin, C. Reitz, P. Hartmann, J. Janek and T. Brezesinski, *Sci. Rep.*, 2019, **9**, 1–11.
42 B. Han, B. Key, A. S. Lipton, J. T. Vaughey, B. Hughes, J. Trevey and F. Dogan, *J. Electrochem. Soc.*, 2019, **166**, A3679–A3684.
43 Y. S. Jung, A. S. Cavanagh, A. C. Dillon, M. D. Groner, S. M. George and S. H. Lee, *J. Electrochem. Soc.*, 2010, **157**, 75–81.
44 P. Yan, J. Zheng, X. Zhang, R. Xu, K. Amine, J. Xiao, J. G. Zhang and C. M. Wang, *Chem. Mater.*, 2016, **28**, 857–863.
45 C. Wang, Y. Zhao, Q. Sun, X. Li, Y. Liu, J. Liang, X. Li, X. Lin, R. Li, K. R. Adair, Z. Li, R. Yang, S. Lu and X. Sun, *Nano Energy*, 2018, **53**, 168–174.
46 L. Sang, K. L. Bassett, F. C. Castro, M. J. Young, L. Chen, R. T. Haasch, J. W. Elam, V. P. Dravid, R. G. Nuzzo and A. A. Gewirth, *Chem. Mater.*, 2018, **30**, 8747–8756.
47 W. S. LePage, Y. Chen, E. Kazyak, K. Chen, A. J. Sanchez, A. Poli, E. M. Arruda, M. D. Thouless and N. P. Dasgupta, *J. Electrochem. Soc.*, 2019, **166**, A89–A97.
48 F. Wu, W. Fitzhugh, L. Ye, J. Ning and X. Li, *Nat. Commun.*, 2018, **9**, 1–11.
49 A. Jain, S. P. Ong, G. Hautier, W. Chen, W. D. Richards, S. Dacek, S. Cholia, D. Gunter, D. Skinner, G. Ceder and K. A. Persson, *APL Mater.*, , DOI:10.1063/1.4812323.
50 Y. Zhu, X. He and Y. Mo, *Adv. Sci.*, 2017, **4**, 1–11.
51 Y. Liu, N. S. Hudak, D. L. Huber, S. J. Limmer, J. P. Sullivan and J. Y. Huang, *Nano Lett.*, 2011, **11**, 4188–4194.
52 S. Hao and C. Wolverton, *J. Phys. Chem. C*, 2013, **117**, 8009–8013.
53 J. S. Park, X. Meng, J. W. Elam, S. Hao, C. Wolverton, C. Kim and J. Cabana, *Chem. Mater.*, 2014, **26**, 3128–3134.
54 S. C. Jung and Y. K. Han, *J. Phys. Chem. Lett.*, 2013, **4**, 2681–2685.
55 K. N. Wood and G. Teeter, *ACS Appl. Energy Mater.*, 2018, **1**, 4493–4504.
56 A. Gupta, E. Kazyak, N. Craig, J. Christensen, N. P. Dasgupta and J. Sakamoto, *J. Electrochem. Soc.*, 2018, **165**, A2801–A2806.
57 K. N. Wood, E. Kazyak, A. F. Chadwick, K.-H. Chen, J.-G. Zhang, K. Thornton and N. P. Dasgupta, *ACS Cent. Sci.*, 2016, **2**, 790–801.
58 B. J. Neudecker, N. J. Dudney and J. B. Bates, *J. Electrochem. Soc.*, 2000, **147**, 517.
59 K. H. Chen, K. N. Wood, E. Kazyak, W. S. Lepage, A. L. Davis, A. J. Sanchez and N. P. Dasgupta, *J. Mater. Chem. A*, 2017, **5**, 11671–11681.
60 K. N. Wood, M. Noked and N. P. Dasgupta, *ACS Energy Lett.*, 2017, **2**, 664–672.
61 M. Schmid, H. P. Steinrück and J. M. Gottfried, *Surf. Interface Anal.*, 2014, **46**, 505–511.

 This journal is © The Royal Society of Chemistry 20xx

Please do not adjust margins